Applied Surface Science 599 (2022) 153766

Contents lists available at ScienceDirect

Applied Surface Science

journal homepage: www.elsevier.com/locate/apsusc

Full Length Article

Spin polarized STM imaging of nanoscale Néel skyrmions in an $SrIrO_3$/$SrRuO_3$ perovskite bilayer

Joseph.P. Corbett [a,b,*], Keng-Yuan Meng [a], Jacob J. Repicky [a], Reyes Garcia-Diaz [c], James.R. Rowland [a], Adam.S. Ahmed [a], Noburo Takeuchi [c], Jonathan Guerrero-Sanchez [c], Fengyuan.Y. Yang [a], Jay.A. Gupta [a]

[a] Department of Physics, the Ohio State University, Columbus, OH 43210, USA
[b] UES Inc., 4401 Dayton-Xenia Rd, Dayton, OH 45432, USA
[c] Centro de Nanociencias y Nanotecnologia, Universidad Nacional Autónoma de México, Apartado Postal 14, Ensenada, Baja California Código Postal 22800, Mexico

ARTICLE INFO

Keywords:
Spin-polarized scanning tunneling microscopy
Perovskite
Complex oxide
Skyrmion
Density functional theory
SIO SRO

ABSTRACT

Oxide heterostructures are an emerging materials platform for engineering the size, stability and motion of magnetic skyrmions in next-generation devices. Here we use off-axis sputtering to grow epitaxial thin films, comprising just two unit cells of $SrIrO_3$ on ten unit cells of the oxide ferromagnet, $SrRuO_3$. Spin polarized scanning tunneling microscopy reveals isolated skyrmions and directly establishes their Néel character, attributed to non-collinear exchange interactions at the interface. Statistical analysis reveals a distribution of sizes and shapes, with an average diameter of 3 nm that is among the smallest reported to date in any system. Skyrmions were only observed in $SrIrO_3$-covered regions of the film, but were otherwise independent of $SrIrO_3$ grain area and thickness. To help explain these observations, we performed density functional theory calculations, which suggest $SrIrO_3$ acquires an induced magnetic moment in proximity to $SrRuO_3$ and thus may host columnar spin textures stabilized by the interface.

1. Introduction

Skyrmions are chiral magnetic textures whose magnetization winds in such a way as to result in a quantized topological charge [1]. Skyrmions are an attractive candidate for next-generation nonvolatile storage and logic as they can be much smaller than conventional magnetic domains, and can be manipulated with lower current densities in devices [2–4]. Such devices require a multi-dimensional materials development effort to optimize the balance of materials parameters that determine Skyrmion size, stability and motion [1,5–7]. For example, the smallest isolated Skyrmions reported to date (~3 nm diameter) have been realized at low temperature in Fe/Ir(111) epitaxial thin films [8,9], while motion in devices has been demonstrated with much larger Skyrmions in sputtered metallic multilayer systems at room temperature [6,7].

Skyrmions can be stabilized from a competition between the ferromagnetic exchange interaction, which favors aligned spins, and the Dzyaloshinskii-Moriya interaction (DMI), which favors perpendicular spins. Interfacial DMI arises from a combination of spin-orbit coupling and broken inversion symmetry at the interface [10]. In this context, the intertwined electronic and magnetic properties of perovskite oxides and the emergent properties of oxide hetero-interfaces [11] and 2D heterostructures [12,13] makes oxides an ideal materials platform for optimization of skyrmions. The perovskite $SrIrO_3$/$SrRuO_3$ bilayer system of interest here combines $SrIrO_3$, which provides strong spin-orbit coupling for large DMI and is non-magnetic in the bulk, and $SrRuO_3$, which is an itinerant ferromagnet with a Curie temperature $T_C > 100$ K. Topological Hall Effect (THE) measurements provided initial evidence for Skymrion formation in $SrIrO_3$/$SrRuO_3$ bilayers [14] and subsequent work demonstrated electric-field control [15]. Given debates in THE interpretation [16], direct imaging of the Skyrmions is important, and subsequent magnetic force microscopy (MFM) imaging directly correlated THE with ~10 nm magnetic bubble formation at similar magnetic field values [17]. These bubbles were at the resolution limit for MFM however, and their topological nature could not be directly confirmed as MFM only probes the out-of-plane component of magnetization.

Here we report spin polarized scanning tunneling microscopy (SPSTM) measurements of isolated skyrmions in $SrIrO_3$/$SrRuO_3$ bilayers

* Corresponding author.
E-mail address: jc362012@ohio.edu (Joseph.P. Corbett).

https://doi.org/10.1016/j.apsusc.2022.153766
Received 3 January 2022; Received in revised form 19 May 2022; Accepted 20 May 2022
Available online 11 June 2022

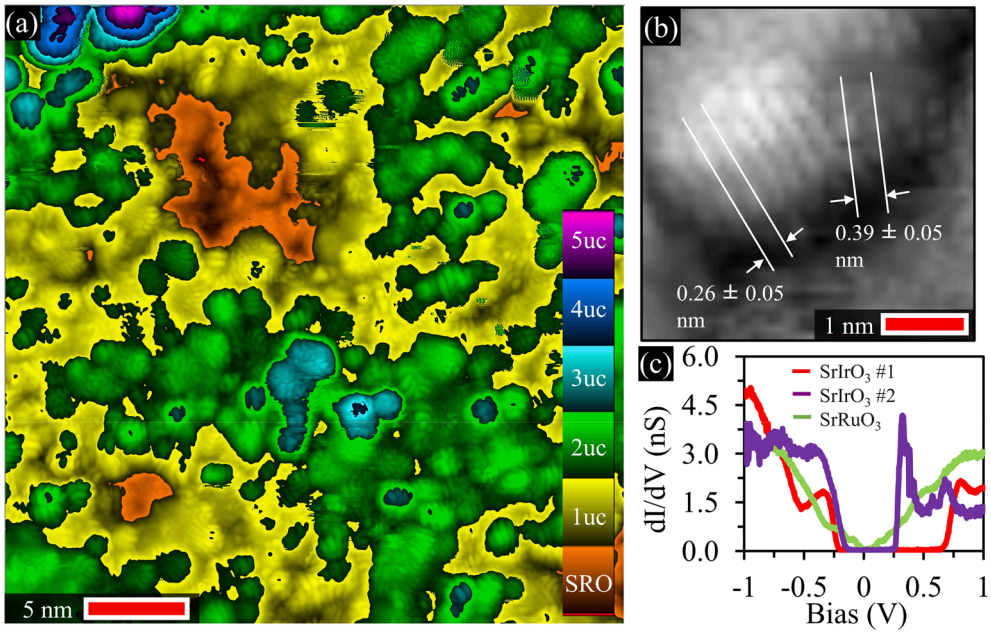

Fig. 1. Identification and morphology of the terminating $SrIrO_3$ layer. (a) STM topographic image showing small grains attributed to $SrIrO_3$ islands. The color scale is discretized by the $SrIrO_3$ unit cell of 0.4 nm (b) Atomic resolution image ~2.5 unit cell island showing lattice fringes consistent with $SrIrO_3$. (c) Tunneling spectroscopy corresponding to two $SrIrO_3$ islands and an exposed $SrRuO_3$ region (c.f. Fig. S2 for locations). STM images were acquired with (−1.5 V, 90 pA), while the tip height was stabilized at (−1 V, 1 nA) in (c).

which indicate an average diameter of ~3 nm, among the smallest reported in any system. The topological Néel character of the skyrmions is directly confirmed by comparing the observed changes in contrast with tip spin orientation or magnetic field with simulated SPSTM images. Isolated skyrmions were only observed in $SrIrO_3$-covered regions of the $SrRuO_3$ film, but were otherwise independent of $SrIrO_3$ grain area and thickness. SPSTM images and density functional theory (DFT) calculations suggest $SrIrO_3$ acquires an induced magnetic moment and thus may host columnar spin textures stabilized by the interface. This study probes a novel regime where both skyrmions and heterostructure have similar nanometer length scales, which will be important for the development of high density magnetic memories.

2. Methods

Sample growth: Epitaxial growth of the $SrIrO_3/SrRuO_3/SrTiO_3$ films was achieved using a custom-built off-axis dc sputtering system [17]. The commercial $SrTiO_3(001)$ substrates were cleaned with a buffered-HF solution for 30 s and subsequently annealed in air for 2 h at 1050 °C. The substrate growth temperature was 420 °C for $SrRuO_3$ and $SrIrO_3$ depositions. An O_2/Ar gas mixture was used for sputtering with a total pressure of 8 mTorr (7 mTorr) with O_2 partial pressures being 96 μTorr (35 μTorr) for $SrRuO_3$ ($SrIrO_3$) deposition. Bilayer epitaxial films were grown with 2 unit cells (u.c.) of $SrIrO_3$ and 10 u.c. of $SrRuO_3$ (1 u.c. ~ 0.39 nm) on a TiO_2 terminated $SrTiO_3$ substrate. Further details of the growth, and characterization of the film and epitaxial interface quality by x-ray diffraction and cross-sectional scanning transmission electron microscopy were reported previously [17].

STM imaging: Following growth, the samples were transferred *ex-situ* to the UHV load lock of a Createc LT-STM system. During this transfer, a mechanical spring clip was positioned to hold the sample and make electrical contact to the top surface. Though standard UHV surface preparation methods (Ar^+ ion sputtering, high temperature annealing) were not used to preserve the as-grown thin films, the samples were annealed under UHV conditions to 120 °C for 1 h to remove adsorbed air containments. The sample was then cooled to 100 K and a ~0.4 T out-of-plane magnetic field was applied to saturate the magnetization of the as-grown film. The magnetic field was removed and the sample then transferred to the cold STM at 5 K. All SP-STM measurements were performed at 5 K using bulk Cr tips which were electrochemically etched and cleaned via cycles of Ar^+ sputtering. The Cr tips are antiferromagnetic, so that the atomic termination of the tip has a preferred spin polarization direction, even though there is no net magnetization of the tip [18]. Tunneling spectra were obtained by disabling the STM feedback loop, adding a modulation voltage (50 mV_{rms}, 1500 Hz) to the DC sample bias, and using a lock in amplifier to measure the corresponding modulation in tunneling current dI/dV as the DC bias was swept. Simultaneous topography and SPSTM images of the dI/dV signal were acquired at fixed voltage while the STM feedback loop was engaged. Image processing and analysis was performed using Gwyddion for STM data [19].

Density Functional Theory: Our spin-polarized total energy calculations are carried out within the DFT framework as developed in the Vienna Ab initio Simulation Package (VASP) [20]. To sample the electron-electron interactions, the generalized gradient approximation as stated by Perdew-Burke-Ernzerhof has been used [21]. Projector augmented-waves were used to treat the core electrons [22]. Electronic states were expanded in plane waves with an energy cutoff of 550 eV. A gamma centered K-points grid of 6x6x1 was used to evaluate the Brillouin zone integration. To evaluate the electronic properties, a denser K-points mesh of 12x12x1 was used.

In order to model the bilayer system, we first determined the most stable lattice parameters for the $SrRuO_3$, and $SrIrO_3$ perovskites in their cubic phase. After structural optimizations, the obtained lattice parameters were 3.97 Å and 4.02 Å, respectively. The $SrRuO_3(001)$ surfaces were constructed by using the supercell method. We then considered the two possible surface terminations, SrO and RuO (we have used slab thickness of 8 and 7 layers, respectively). A vacuum space of 15 Å was used to preclude surface self-interactions on both models. Once optimized, we proceed to place on top two $SrIrO_3$ unit cells, with its lattice parameter set to match the $SrRuO_3$ substrate. Two possible surface terminations again emerge, Sr-O and Ir-O and we utilize 12 and 13 layers respectively with the same 15 Å vacuum space.

3. Results and discussion

STM images of the $SrIrO_3/SrRuO_3$ bilayer sample reveal large, atomically-flat areas covered by a densely packed network of islands (Fig. 1a). The color scale in Fig. 1a is discretized in terms of the 0.39 nm $SrIrO_3$ unit cell (u.c.), and shows that most of the surface exhibits apparent heights corresponding to 1–2 u.c. with respect to the lowest

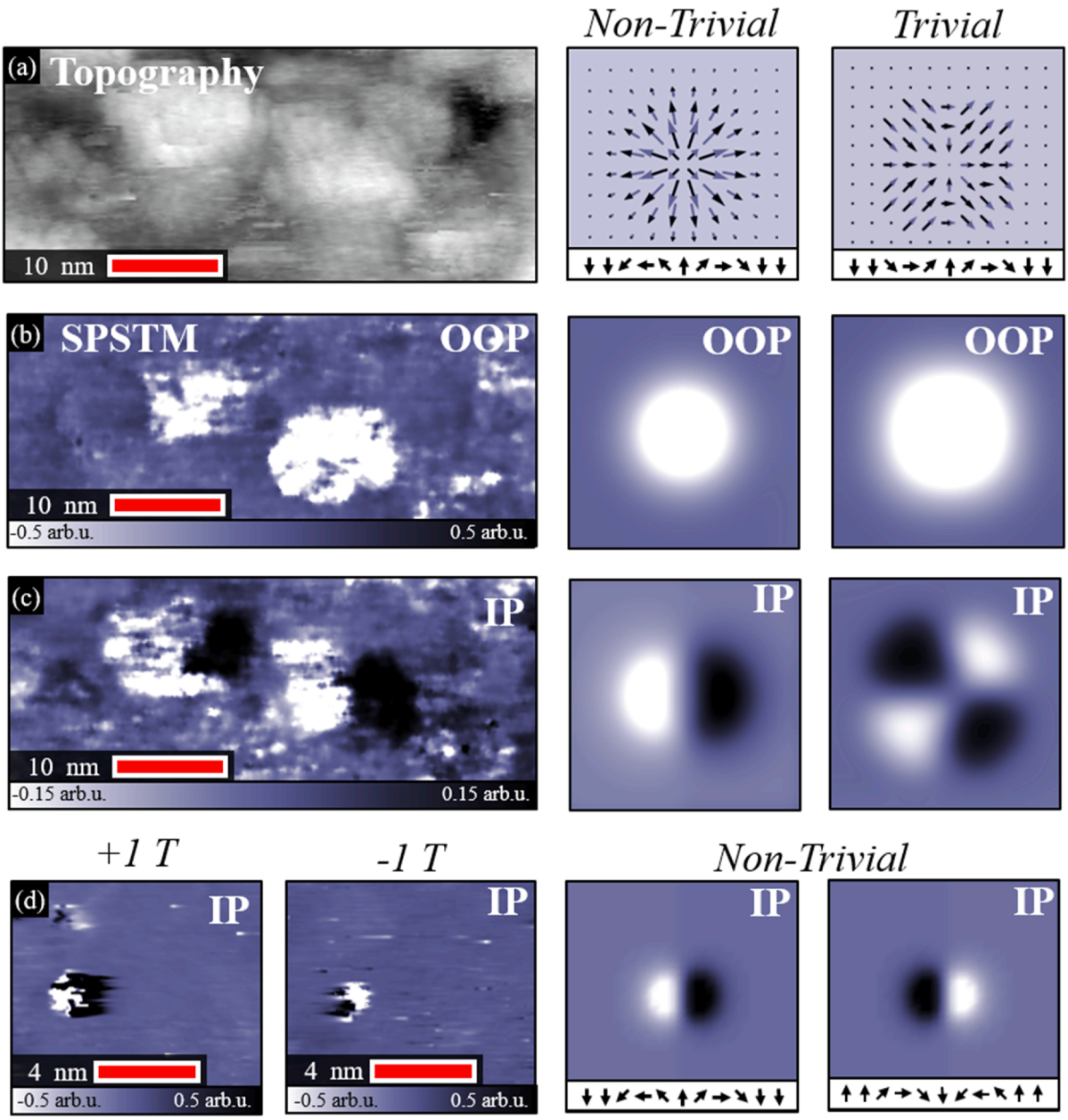

Fig. 2. Comparison of experimental and simulated SPSTM images of Neél skyrmions. (a) Left - Topographic STM image showing ~3 unit cell thick $SrIrO_3$ grains. Right - magnetization maps for trivial and non-trivial Neél-like spin textures. (b) Left - SPSTM image simultaneously acquired with (a), showing bright contrast attributed to two skyrmions localized to $SrIrO_3$ grains and imaged with a tip sensitive to out-of-plane (OOP) magnetization. Right – simulated SPSTM images for trivial and non-trivial Neél textures with an OOP tip. (c) Left – SPSTM image of the same area, but with a tip sensitive to in-plane magnetization (IP tip). Right – simulated SPSTM images with an IP tip showing good agreement for non-trivial Neél skyrmions. (d) SPSTM image of another skyrmion in a different area, showing reversal in the lobed contrast with ±1 T magnetic field applied out of the plane. Right – SPSTM simulations for a Neél skrymion in magnetic field. (a-c) acquired with (−1 V, 300 pA), (d) acquired with (−1.5 V, 90 pA).

points in the image. This is consistent with the nominal 2 u.c. $SrIrO_3$ film thickness, and fringe-like contrast on these islands (Fig. 1b) is consistent with $SrIrO_3$ atomic spacings as well. Tunneling conductance (dI/dV) spectra further distinguish between $SrIrO_3$ and $SrRuO_3$ regions (Fig. 1c). In regions with the darkest contrast (orange in Fig. 1a), we observe a small dip near 0 V with gradually increasing conductance on either side (Fig. 1c, green curve). This spectrum is similar to control STM measurements on the bare $SrRuO_3$ film (c.f. Supporting Information) and recent STM studies [23], and is consistent with the metallic density of states of $SrRuO_3$ from DFT calculations [24]. In contrast, tunneling spectra taken on the bright islands show a well-developed 0.5–1 V gap, depending on the island thickness (Fig. 1c, purple and red curves). This insulating behavior is consistent with thin film transport studies showing a transition from semi-metal to insulating states for $SrIrO_3$ films < 4 u.c. thick [25–28].

SPSTM images of skyrmions were acquired by spatially mapping the differential tunneling conductance, dI/dV, given by the following equation:

$$\frac{dI}{dV}(\pm V) \propto n_s n_t(E_F \pm eV) + P_s P_t(E_F \pm eV)\cos(\overrightarrow{m_t}, \overrightarrow{m_s}) \quad (1)$$

where V is the bias voltage, n_s (n_t) is the sample (tip) density of states, P_s (P_t) is the sample (tip) spin polarization, and the cosine term depends on the angle between the local sample and tip magnetization unit vectors

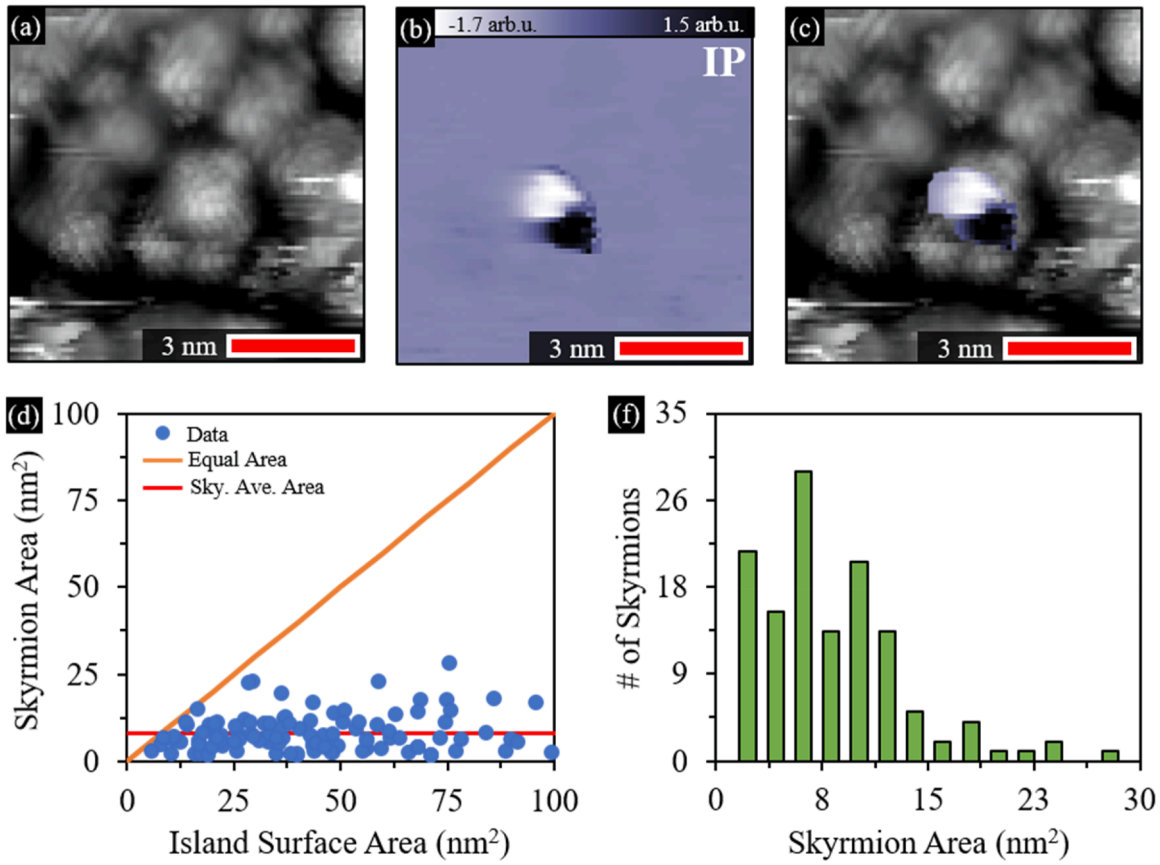

Fig. 3. Correlation of nanoscale Neél skyrmions with $SrIrO_3$ grains. (a) STM topographic image of few-nm $SrIrO_3$ grains. (b) Simultaneous SPSTM image, showing lobed contrast of a <2 nm Neél skyrmion imaged with an IP tip. (c) overlay of the topographic and SPSTM images, showing the skyrmion is localized to an individual 2 unit cell thick $SrIrO_3$ island. (d) plot comparing skyrmion areas and corresponding $SrIrO_3$ island areas. The orange line indicates equal areas; all data points fall below this line, indicating that skyrmion area is independent of $SrIrO_3$ island size, except in the very smallest islands. The red line indicates the average skyrmion area of 8 nm^2. (e) Histogram of skyrmion sizes.

$\boldsymbol{m_s}$, $\boldsymbol{m_t}$ [18]. The first term represents the contribution from the electronic density of states, while the second term represents the magnetic contribution if a tip with spin sensitivity is used (i.e., bulk Cr in our case). Because not all spin textures are topologically non-trivial [29–31], we consider both non-trivial Néel skymrion textures and a Néel-like trivial bubble, formed by combining two Néel domain walls along a line (Fig. 2a) [32]. In both cases, the core magnetization of the texture is chosen opposite to the ferromagnetic background, which points out of plane due to uniaxial magnetic anisotropy [17]. We then simulate SPSTM images using Eq. (1) for tips sensitive to out-of-plane (OOP) and in-plane (IP) magnetization, which allows us to distinguish between these candidate spin textures [32].

For the two $SrIrO_3$ islands shown in the STM topography image (Fig. 2a), the corresponding SPSTM map (Fig. 2b) reveals a uniform background and two regions of bright contrast < 10 nm in diameter. This image agrees well with SPSTM simulations for a tip sensitive to out-of-plane magnetization, but cannot distinguish between non-trivial and trivial Néel textures as both would be imaged with bright contrast (Fig. 2b, right panels). To unambiguously identify the topological nature of these textures, it is necessary to image them with a tip sensitive to in-plane magnetization (IP tip) [32], and with applied magnetic field. In SP-STM experiments, the atomic termination of the tip can change as a result of interactions with the surface during repeated imaging [33]. Fig. 2c shows an SPSTM map of the same two textures with a different atomic tip termination but under otherwise identical imaging conditions. The textures now exhibit a lobed structure, with a bright side above the background, and a dark side that is below the background. The switching of contrast to bright/dark lobed structures is consistent with the simulated SPSTM image for a Néel Skyrmion with an in-plane tip, while a more complicated clover pattern would be expected for the trivial bubble. Because the interfacial DMI selects a handedness for the winding of the magnetization, an applied magnetic field is expected to invert each spin within the skyrmion texture and thus the overall double-lobe contrast [33]. Fig. 2d shows such an inversion for another, 2 nm Skyrmion imaged with an IP tip and ±1 T out-of-plane magnetic field. This field is too small to polarize the ferromagnetic $SrRuO_3$ film in its entirety [17] or affect the antiferromagnetic Cr tip [18]. However, the local domain can flip with these fields, leading to a reversal in the lobed contrast for the skyrmion as well, since the core is anti-parallel to the local ferromagnetic background. The switching of contrast with tip orientation and magnetic field in Fig. 2 allows us to rule out electronic contributions to the measured dI/dV signal, and unambiguously identify these textures as Néel Skyrmions stabilized by interfacial DMI.

To explore the critical role of the interface in providing the necessary DMI, we note that skyrmions were never observed in regions where the underlying ferromagnetic $SrRuO_3$ layer was exposed (e.g., orange regions in Fig. 1a) or in control measurements on $SrRuO_3$ films (c.f. supporting information). To better understand the association with $SrIrO_3$, we compiled a statistical analysis comparing skyrmion sizes and their host $SrIrO_3$ islands. Fig. 3a-b show topography and SPSTM images indicating a skyrmion localized to one $SrIrO_3$ island in the center of the image. By overlaying these two images (Fig. 3c), we observe that while the skymrion is associated with a particular $SrIrO_3$ island, it's spatial extent doesn't exactly trace the island's topography. Using a masking procedure discussed in the supporting information, we extract an average area of the $SrIrO_3$ islands from STM topographic images, and

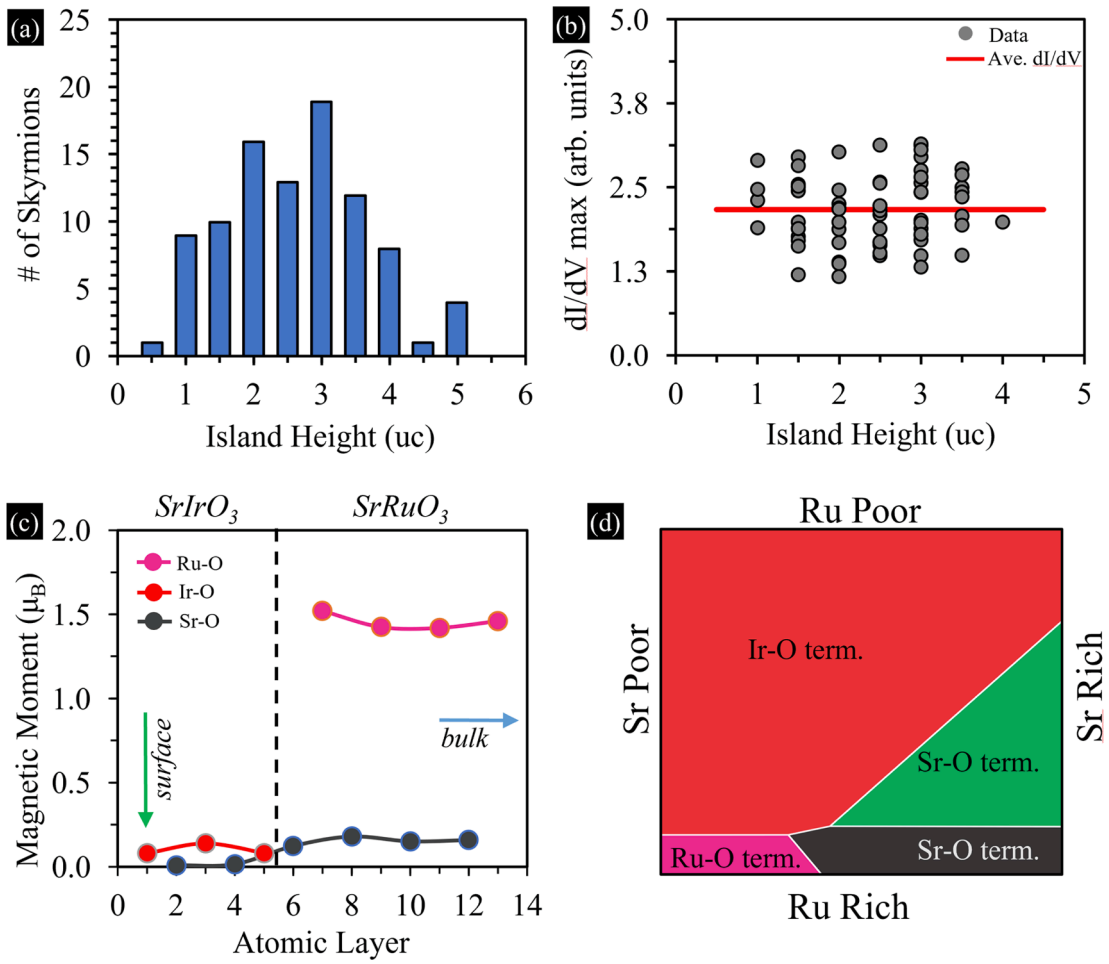

Fig. 4. (a) Histogram of skyrmions and $SrIrO_3$ island heights, showing a peak near the nominal 2 u.c. film thickness. (b) plot of skyrmion dI/dV contrast taken with an OOP tip versus $SrIrO_3$ island height. Because SPSTM is surface sensitive, the absence of a pronounced dependence on separation from the ferromagnetic $SrRuO_3$ layer is suggestive of skyrmions being hosted in the $SrIrO_3$ itself. (c) DFT calculations of the computed magnetic moment per atomic layer for an IrO-terminated $SrIrO_3$/$SrRuO_3$ heterostructure. A small induced moment is indicated on IrO layers in the $SrIrO_3$ film. (d) DFT-calculated phase diagram of the energetically favored surface termination under varying Sr, Ru growth conditions.

their associated skyrmions from SPSTM images. The results of this analysis in Fig. 3d indicate that while at the lower end (<10 nm^2), skyrmions may be limited by the size of the host island, the skyrmion size is independent of area for larger islands. Since all data points fall below the equal-area line in Fig. 3d, the skyrmions are never larger than the associated $SrIrO_3$ island. A histogram of skyrmion sizes is plotted in Fig. 3(e) and gives an average skyrmion area of 8.0 ± 5.0 nm^2 (~3.2 nm diameter if circular) and a mode of 6.0 nm^2. The distribution is slightly positively skewed, reflecting the physical limit imposed by the finite island size at the lower end of the distribution.

The material or magnetic characteristics that limit the density of skyrmions is an important question that can be addressed in SPSTM measurements. For example, why does only one $SrIrO_3$ island in Fig. 3 host a skyrmion while the others do not? To help answer such questions, we compiled a histogram of skyrmions versus thickness of the host $SrIrO_3$ island in Fig. 4a. The peak in the distribution between 2 and 3 u.c. matches the statistical distribution of the islands themselves (c.f. supporting information), suggesting that there is no preferred $SrIrO_3$ layer thickness that stabilizes skyrmions in this range. Because SPSTM is surface sensitive, we would also expect an exponential decay of the SPSTM signal with $SrIrO_3$ layer thickness if the skyrmions were hosted solely in the underlying ferromagnetic $SrRuO_3$ layer. However, the dI/dV signal associated with the skyrmion contrast appears roughly independent of island thickness (Fig. 4b), within the experimental uncertainty caused by changes in tip spin sensitivity and local environments. This suggests that the spin textures may be more columnar-like and extend through both $SrIrO_3$ and $SrRuO_3$ layers in the bilayer system.

To explore this possibility, we performed spin-polarized DFT calculations of the $SrIrO_3$/$SrRuO_3$ bilayer system (c.f. Supporting Information for more details). While bulk $SrIrO_3$ is a paramagnetic semi-metal, the interplay of strong electronic correlations and spin-orbit coupling may lead to layer-dependent properties in few-layer thin films, including induced magnetic order, such as spin-glass, ferromagnetic, and antiferromagnetic states [34–37]. As shown in Fig. 4c, in the 10 u.c. ferromagnetic $SrRuO_3$ film, we find that the magnetic moment (μ_B) per atomic layer primarily lies within the RuO planes (1.5 μ_B/Ru), with a much smaller induced moment on the SrO planes (~0.3 μ_B/Sr). In agreement with prior STEM measurements on these samples [29], our total energy calculations suggest that SrO is the preferred terminating layer at the interface with $SrIrO_3$. We find a similar induced moment on the IrO planes in the overlying $SrIrO_3$ film (0.1–0.2 μ_B/Ir), also in agreement with previous DFT [38–40]. While this moment persists for all IrO planes in the $SrIrO_3$ film, the induced moment in the SrO planes in $SrIrO_3$ falls quickly to zero away from the $SrRuO_3$ interface. DFT total-energy calculations with varying chemical potential suggest that the magnetic IrO termination is preferred over most of the Sr/Ru phase space, but SrO terminations may also be possible (Fig. 4d and c.f. supporting information).

These DFT calculations help reconcile the surface sensitivity of SPSTM with the observed associations with the $SrIrO_3$ overlayer. First,

an induced moment in the $SrIrO_3$ could lead to more columnar-like Néel skyrmions that are stabilized by DMI from the $SrIrO_3/SrRuO_3$ interface. This could explain why our SPSTM data reveal magnetic contrast even though the underlying ferromagnetic $SrRuO_3$ is not at the surface. Secondly, the induced moment is likely sensitive to the interfacial structure, and combined with the possibility of non-magnetic SrO terminations, may explain why we observe skyrmions on only a fraction of the $SrIrO_3$ islands. It will be of interest to extend these first-principles calculations in future studies to estimate magnetic parameters such as DMI to gain further insights correlating structure with the nanoscale skyrmions measured here.

In conclusion, we report SPSTM imaging directly confirming Néel skyrmions in $SrIrO_3$/ $SrRuO_3$ bilayers that are among the smallest reported for any material to date. This study probes a novel regime where both skyrmions and heterostructure have similar nanometer length scales, which will be important for the development of high density magnetic memories. Though beyond the scope of this initial study, we note that switching dynamics of some skyrmions was observed as noise in repeated SP-STM imaging with varying STM currents and pulsing (c.f. Supporting Information). These dynamics, coupled with the broad tunability of oxide systems and their interfaces, is particularly promising for future devices.

CRediT authorship contribution statement

J.P.C: conceptualization, data curation, formal analysis, investigation, methodology, visualization, writing-original draft, writing-review & editing. **J.J.R:** data curation, methodology, writing-review & editing. **J.R.R:** formal analysis, software supervision, and writing-review & editing. **K.-Y.M:** Investigation. **A.S.A:** investigation, methodology, writing-review & editing. **R.G.-D:** formal analysis, investigation, methodology, software supervision, and writing review & editing. **N.T:** formal analysis, investigation, methodology, software supervision, and writing review & editing. **J.G.-S:** formal analysis, investigation, methodology, software supervision, and writing review & editing. **F.Y.Y.** conceptualization, formal analysis, funding acquisition, project administration, and writing-review & editing. **J.A.G:** conceptualization, formal analysis, funding acquisition, project administration, and writing-review & editing.

Declaration of Competing Interest

The authors declare that they have no known competing financial interests or personal relationships that could have appeared to influence the work reported in this paper.

Acknowledgements

We acknowledge primary support from the Defense Advanced Research Projects Agency under Grant No. D18AP00008 (SPSTM imaging and analysis) and the Center for Emergent Materials, an NSF MRSEC, under Grant No. DMR-2011876 (film growth and characterization). R.G.-D., N.T. and J.G.-S. thank DGAPA-UNAM projects IN101019 and IA100822, and CONACyT grant A1-S9070 of the Call of Proposals for Basic Scientific Research 2017-2018 for partial financial support. Calculations were performed in the DGCTIC-UNAM Supercomputing Center, project LANCAD-UNAMDGTIC-051 and LANCAD-UNAMDGTIC-368.

Appendix A. Supplementary data

Supplementary data to this article can be found online at https://doi.org/10.1016/j.apsusc.2022.153766.

References

[1] Y. Tokura, N. Kanazawa, Magnetic Skyrmion Materials, Chem. Rev. 121 (2021) 2857–2897.
[2] R. Tomasello, E. Martinez, R. Zivieri, L. Torres, M. Carpentieri, G. Finocchio, A strategy for the design of skyrmion racetrack memories, Sci. Rep. 4 (1) (2015).
[3] A. Fert, V. Cros, J. Sampaio, Skyrmions on the track, Nat. Nanotechnol. 8 (3) (2013) 152–156.
[4] S. Luo, L. You, Skyrmion devices for memory and logic applications, APL Mater. 9 (5) (2021) 050901.
[5] R. Wiesendanger, Nanoscale magnetic skyrmions in metallic films and multilayers: a new twist for spintronics, Nat. Rev. Mater. 1 (2016) 1–11.
[6] A. Fert, N. Reyren, V. Cros, Magnetic skyrmions: advances in physics and potential applications, Nat. Rev. Mater. 2 (2017) 17031.
[7] W. Jiang, et al., Skyrmions in magnetic multilayers, Phys. Rep.-Rev. Sec. Phys. Lett. 704 (2017) 1–49.
[8] N. Romming, C. Hanneken, M. Menzel, J.E. Bickel, B. Wolter, K. von Bergmann, A. Kubetzka, R. Wiesendanger, Writing and Deleting Single Magnetic Skyrmions, Science 341 (6146) (2013) 636–639.
[9] P.-J. Hsu, A. Kubetzka, A. Finco, N. Romming, K. von Bergmann, R. Wiesendanger, Electric-field-driven switching of individual magnetic skyrmions, Nat. Nanotechnol. 12 (2) (2017) 123–126.
[10] S. Mühlbauer, B. Binz, F. Jonietz, C. Pfleiderer, A. Rosch, A. Neubauer, R. Georgii, P. Böni, Skyrmion Lattice in a Chiral Magnet, Science 323 (5916) (2009) 915–919.
[11] H.Y. Hwang, Y. Iwasa, M. Kawasaki, B. Keimer, N. Nagaosa, Y. Tokura, Emergent phenomena at oxide interfaces, Nat. Mater. 11 (2) (2012) 103–113.
[12] D. Ji, S. Cai, T.R. Paudel, H. Sun, C. Zhang, L.u. Han, Y. Wei, Y. Zang, M. Gu, Y. i. Zhang, W. Gao, H. Huyan, W. Guo, D.i. Wu, Z. Gu, E.Y. Tsymbal, P. Wang, Y. Nie, X. Pan, Freestanding crystalline oxide perovskites down to the monolayer limit, Nature 570 (7759) (2019) 87–90.
[13] A.G. Ricciardulli, S. Yang, J.H. Smet, M. Saliba, Emerging perovskite monolayers, Nat. Mater. 20 (10) (2021) 1325–1336.
[14] J. Matsuno, N. Ogawa, K. Yasuda, F. Kagawa, W. Koshibae, N. Nagaosa, Y. Tokura, M. Kawasaki, Interface-driven topological Hall effect in SrRuO3-SrIrO3 bilayer, Sci. Adv. 2 (7) (2016) e1600304.
[15] Y. Ohuchi, J. Matsuno, N. Ogawa, Y. Kozuka, M. Uchida, Y. Tokura, M. Kawasaki, Electric-field control of anomalous and topological Hall effects in oxide bilayer thin films, Nat. Commun. 9 (1) (2018).
[16] D. Kan, T. Moriyama, K. Kobayashi, Y. Shimakawa, Alternative to the topological interpretation of the transverse resistivity anomalies in ${\mathrm{SrRuO}}_{3}$, Phys. Rev. B 98 (2018) 180408.
[17] K.-Y. Meng, A.S. Ahmed, M. Baćani, A.-O. Mandru, X. Zhao, N. Bagués, B.D. Esser, J. Flores, D.W. McComb, H.J. Hug, F. Yang, Observation of Nanoscale Skyrmions in SrIrO3/SrRuO3 Bilayers, Nano Lett. 19 (5) (2019) 3169–3175.
[18] R. Wiesendanger, Spin mapping at the nanoscale and atomic scale, Rev. Mod. Phys. 81 (4) (2009) 1495–1550.
[19] D. Nečas, P. Klapetek, Gwyddion: an open-source software for SPM data analysis, Open Phys. 10 (2012).
[20] G. Kresse, J. Furthmüller, Efficient iterative schemes for *ab initio* total-energy calculations using a plane-wave basis set, Phys. Rev. B 54 (16) (1996) 11169–11186.
[21] J.P. Perdew, K. Burke, M. Ernzerhof, Generalized Gradient Approximation Made Simple, Phys. Rev. Lett. 77 (18) (1996) 3865–3868.
[22] P.E. Blöchl, Projector augmented-wave method, Phys. Rev. B 50 (24) (1994) 17953–17979.
[23] H.G. Lee, L. Wang, L. Si, X. He, D.G. Porter, J.R. Kim, E.K. Ko, J. Kim, S.M. Park, B. Kim, A.T.S. Wee, A. Bombardi, Z. Zhong, T.W. Noh, Atomic-Scale Metal-Insulator Transition in SrRuO3 Ultrathin Films Triggered by Surface Termination Conversion, Adv. Mater. 32 (8) (2020) 1905815.
[24] G. Koster, et al., Structure, Physical Properties, and Applications of SrRuO3 Thin Films, Rev. Mod. Phys. 84 (2012) 253–298.
[25] F.-X. Wu, J. Zhou, L.Y. Zhang, Y.B. Chen, S.-T. Zhang, Z.-B. Gu, S.-H. Yao, Y.-F. Chen, Metal-Insulator Transition in SrIrO3 with Strong Spin-Orbit Interaction, J. Phys.: Condens. Matter 25 (12) (2013) 125604.
[26] A. Biswas, K.-S. Kim, Y.H. Jeong, Metal Insulator Transitions in Perovskite SrIrO3 Thin Films, J. Appl. Phys. 116 (21) (2014) 213704.
[27] P. Schütz, et al., Dimensionality-Driven Metal-Insulator Transition in Spin-Orbit-Coupled SrIrO 3, Phys. Rev. Lett. 119 (2017).
[28] D.J. Groenendijk, et al., Spin-Orbit Semimetal SrIrO 3 in the Two-Dimensional Limit, Phys. Rev. Lett. 119 (2017) 256403.
[29] Z. Hou, W. Ren, B. Ding, G. Xu, Y. Wang, B. Yang, Q. Zhang, Y. Zhang, E. Liu, F. Xu, W. Wang, G. Wu, X. Zhang, B. Shen, Z. Zhang, Observation of Various and Spontaneous Magnetic Skyrmionic Bubbles at Room Temperature in a Frustrated Kagome Magnet with Uniaxial Magnetic Anisotropy, Adv. Mater. 29 (29) (2017) 1701144.
[30] X. Yu, Y. Tokunaga, Y. Taguchi, Y. Tokura, Variation of Topology in Magnetic Bubbles in a Colossal Magnetoresistive Manganite, Adv. Mater. 29 (3) (2017) 1603958.
[31] X. Yu, M. Mostovoy, Y. Tokunaga, W. Zhang, K. Kimoto, Y. Matsui, Y. Kaneko, N. Nagaosa, Y. Tokura, Magnetic stripes and skyrmions with helicity reversals, Proc. Natl. Acad. Sci. 109 (23) (2012) 8856–8860.
[32] K. Palotás, L. Rózsa, E. Simon, L. Udvardi, L. Szunyogh, Spin-polarized scanning tunneling microscopy characteristics of skyrmionic spin structures exhibiting various topologies, Phys. Rev. B 96 (2) (2017).

[33] N. Romming, A. Kubetzka, C. Hanneken, K. von Bergmann, R. Wiesendanger, Field-Dependent Size and Shape of Single Magnetic Skyrmions, Phys. Rev. Lett. 114 (17) (2015).
[34] J. Nichols, X. Gao, S. Lee, T.L. Meyer, J.W. Freeland, V. Lauter, D.i. Yi, J. Liu, D. Haskel, J.R. Petrie, E.-J. Guo, A. Herklotz, D. Lee, T.Z. Ward, G. Eres, M. R. Fitzsimmons, H.N. Lee, Emerging Magnetism and Anomalous Hall Effect in Iridate-Manganite Heterostructures, Nat. Commun. 7 (1) (2016).
[35] D.i. Yi, J. Liu, S.-L. Hsu, L. Zhang, Y. Choi, J.-W. Kim, Z. Chen, J.D. Clarkson, C. R. Serrao, E. Arenholz, P.J. Ryan, H. Xu, R.J. Birgeneau, R. Ramesh, Atomic-scale control of magnetic anisotropy via novel spin–orbit coupling effect in La $_{2/3}$ Sr $_{1/3}$ MnO $_3$ /SrIrO $_3$ superlattices, Proc. Natl. Acad. Sci. 113 (23) (2016) 6397–6402.
[36] V.V. Demidov, N.V. Andreev, T.A. Shaikhulov, G.A. Ovsyannikov, Observation of Ferromagnetism in a Thin SrIrO3 Film Contacting with a La0.7Sr0.3MnO3 Film, J. Magn. Magn. Mater. 497 (2020) 165979.
[37] B. Pang, et al., Spin-Glass-Like Behavior and Topological Hall Effect in SrRuO3/SrIrO3 Superlattices for Oxide Spintronics Applications, ACS Appl. Mater. Interfaces 9 (2017) 3201–3207.
[38] W. Fan, S. Yunoki, Electronic and Magnetic Structure Under Lattice Distortion in SrIrO3 /SrTiO3 Superlattice: A First-Principles Study, J. Phys. Conf. Ser. 592 (2015) 012139.
[39] K.-H. Kim, H.-S. Kim, M.J. Han, Electronic Structure and Magnetic Properties of Iridate Superlattice SrIrO3/SrTiO3, J. Phys.: Condens. Matter 26 (2014) 185501.
[40] T.R. Dasa, L. Hao, J. Yang, J. Liu, H. Xu, Strain Effects on Structural and Magnetic Properties of SrIrO3/SrTiO3 Superlattice, Mater. Today Phys. 4 (2018) 43–49.